A Journal of the Gesellschaft Deutscher Chemiker

Angewandte International Edition

GDCh

Chemie

www.angewandte.org

Accepted Article

Title: Pt/MnO2 Nanoflowers Anchored to Boron Nitride Aerogels for Highly Efficient Enrichment and Catalytic Oxidation of Formaldehyde at Room Temperature

Authors: Dongyun Chen, Guping Zhang, Mengmeng Wang, Najun Li, Qingfeng Xu, Hua Li, Jinghui He, and Jian-Mei Lu

To be cited as: *Angew. Chem. Int. Ed.* 10.1002/anie.202013667

Link to VoR: https://doi.org/10.1002/anie.202013667

WILEY-VCH

10.1002/anie.202013667

WILEY-VCH

Pt/MnO_2 Nanoflowers Anchored to Boron Nitride Aerogels for Highly Efficient Enrichment and Catalytic Oxidation of Formaldehyde at Room Temperature

Dongyun Chen, Guping Zhang, Mengmeng Wang, Najun Li, Qingfeng Xu, Hua Li, Jinghui He, and Jianmei Lu*

Abstract: The catalytic room temperature oxidation of formaldehyde (HCHO) is widely considered as a viable method for the abatement of indoor toxic HCHO pollution. Herein, Pt/MnO_2 nanoflowers anchored to boron nitride aerogels (Pt/MnO_2-BN) were fabricated for the catalytic room temperature oxidation of HCHO. The three-dimensional Pt/MnO_2-BN aerogels demonstrated superior catalytic activity as a result of the improved diffusion of the reactant molecules within the porous structure. Furthermore, the porous aerogels displayed excellent HCHO adsorption capacities, which promote a rapid HCHO gas-phase concentration reduction and a subsequent complete oxidation of the adsorbed HCHO. The combined adsorption and oxidation properties of the Pt/MnO_2-BN aerogels synergistically enhance the oxidative removal of HCHO. The optimized Pt/MnO_2-BN demonstrated excellent catalytic activity toward HCHO (200 ppm) at room temperature, achieving a 96% formaldehyde conversion after 50 min.

Indoor living, studying and working accounts for approximately 75% of people's time, and hence, indoor air quality is essential to human health. Therefore, there has been a wealth of interdependent research in recent years focusing on improvements to indoor air quality.[1] Volatile organic compounds (VOCs) are typical indoor air pollutants, which are principally emitted from used building and decorative materials.[2] Particularly, formaldehyde (HCHO) is widely considered as a hazardous VOC that is a significant threat to human health. Long-term continuous exposure to HCHO can result in numerous serious health problems, including respiratory diseases, skin irritation, and cancer.[3] Hence, efficiently removing indoor air HCHO is vital to meet air quality requirements and to reduce public health risks.

Numerous techniques for HCHO removal have been developed over the past few decades, to include physical adsorption, chemical adsorption, photocatalytic degradation, plasma oxidation and thermal catalytic oxidation.[4] Among these aforementioned techniques, adsorption is considered as a feasible and convenient strategy because of improved techno-economics and ease of operation. Numerous adsorbents including activated carbon (AC), AlOOH, and CeO_2 have been investigated with respect to their ability to remove gaseous HCHO.[5] However, even through surface modification or as a component in composite materials, the uptake capacities remain unsatisfactory. From the perspective of the HCHO polarity, materials possessing large specific surface areas and hydrophilic surfaces typically act as excellent adsorbents for HCHO removal.[6] Recently, hexagonal boron nitride (BN), as a graphene analogue, has received extensive research interest in the fields of environmental remediation and solar energy conversion owing to hexagonal BN possessing unique properties such as a two-dimensional (2D) layered structure, a large specific surface area, excellent electrical insulation, and high thermal conductivity.[7] In addition to the large specific surface area, BN possesses high hydrophilicity, and the adsorption of HCHO molecules onto BN has also been theoretically studied.[6b] Therefore, porous BN is expected to demonstrate good adsorption performance toward gaseous HCHO. However, the maximum capacity of the adsorbent and hazards associated with desorption during the regeneration process hinders the effectiveness of adsorbents. Conversely, catalytic oxidation can continuously and completely covert gaseous HCHO into harmless CO_2 and H_2O.[4e-f]

Principally, there are two catalyst family types for HCHO oxidation, including supported noble metals (Pt, Au, Rh and Pd)[8] and non-noble metal oxides (Ag, Co, Ce and Mn).[9] The supported noble metal catalysts, such as alkali-metal-doped Na-Pt/TiO_2,[10a] Pt/MnO_x-CeO_2,[10b] TiO_2-supported Pd nanoparticles (NPs)[8c] and Na promoted Pd/TiO_2,[10c] exhibit outstanding catalytic performance at ambient temperatures, even at high space velocities. Additionally, Mn-based catalysts, such as MnO_x-CeO_2, MnO_x/AC and graphene-MnO_2,[11] have been extensively studied for HCHO oxidation and are the most active catalysts among the transition metal oxides. Moreover, combining the advantages of catalytic oxidation with adsorption nanomaterials could enhance the efficiency of HCHO treatment.

Herein, Pt NPs (~30 nm) were first loaded onto MnO_2 nanoflowers. The Pt NPs provide unique spatial characteristics for the MnO_2 nanoflowers, thereby providing stability to the structure, thus circumventing the disadvantages of aggregation. Thereafter, the as-prepared Pt/MnO_2 composites were dispersed and anchored onto porous aerogels possessing interconnected networks assembled on curled BN nanosheets (**Scheme S1**). The porous structure of the aerogels facilitates HCHO enrichment at the Pt/MnO_2-BN interface and subsequently promotes the complete oxidation of the adsorbed HCHO.

X-ray diffraction (XRD) analysis was undertaken to determine the crystal structures of the as-prepared Pt/MnO_2, series of Pt/MnO_2-BN and BN samples. We prepared a series of Pt/MnO_2-BN (dosage of the Pt/MnO_2 solution: 10, 20 and 40 μL), which were abbreviated as Pt/MnO_2-BN10, Pt/MnO_2-BN20, Pt/MnO_2-BN40, respectively. The diffraction peaks associated with BN, presented in **Figure S1**, are in good agreement with hexagonal BN (JCPDS card No. 45-0893).[6b] Furthermore, the XRD patterns of the Pt/MnO_2 composites exhibit four typical diffraction

[*] Prof. D. Y. Chen, G. P. Zhang, M. M. Wang, Prof. N. J. Li, Prof. Q. F. Xu, Prof. H. Li, Prof. J. H. He, Prof. J. M. Lu
College of Chemistry, Chemical Engineering and Materials Science
Collaborative Innovation Center of Suzhou Nano Science and Technology
Soochow University
Suzhou 215123 (P. R. China)
E-mail: lujm@suda.edu.cn

Supporting information for this article is given via a link at the end of the document.

peaks, which correspond to the (002), (100), (111) and (200) crystalline planes of hexagonal δ-MnO_2.[12] No obvious XRD peaks attributed to the Pt NPs are observed because of the low Pt loadings. Additionally, the peak associated with the (111) crystal plane of MnO_2 is observed in all the Pt/MnO_2-BN aerogel materials. The (111) peak intensity increases as a function of the Pt/MnO_2 composite amount in the aerogel materials. The aforementioned results indicate that the Pt/MnO_2 composites were successfully anchored to the BN aerogels, and furthermore, that all the prepared samples demonstrate a high degree of crystallinity with no impurity diffraction peaks observed.

To confirm the presence of Pt NPs in the Pt/MnO_2 composites and Pt/MnO_2-BN samples, both scanning electron microscopy (SEM) and transmission electron microscopy (TEM) were performed to investigate the morphologies and structures of the as-prepared catalysts. As exhibited in **Figure 1a**, the Pt NPs were first successfully prepared with diameters of ~30 nm. Additionally, the Pt NPs were observed to be aggregates comprising smaller nanoclusters. **Figure 1b** shows that the MnO_2 nanoflowers form a 3D scaffold, which provides a suitable environment for Pt NP loading. Additionally, lattice fringes having spacings of 0.240 nm, 0.290 nm and 0.480 nm are also observed, which correspond to the (100), (020) and (110) crystal planes of MnO_2, respectively (**Figure 1c–d**).[12-13] Furthermore, high-angle annular dark-field scanning transmission microscopy and the corresponding energy dispersive x-ray spectroscopy elemental mapping images (**Figure 1e**) of a single Pt/MnO_2 composite further suggest the existence of Pt NPs in the Pt/MnO_2 composites.

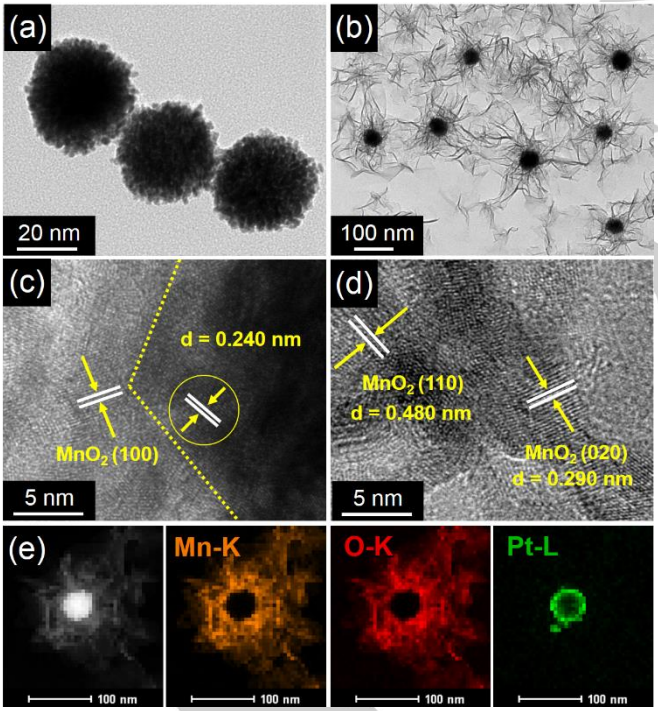

Figure 1. Transmission electron microscopy (TEM) images of (a) Pt nanoparticles and (b) Pt/MnO_2 composites. High resolution TEM micrographs of (c–d) Pt/MnO_2 composites. (e) High-angle annular dark-field scanning transmission microscopy and energy dispersive X-ray spectroscopy elemental mapping images of Mn, O and Pt of the Pt/MnO_2 composites.

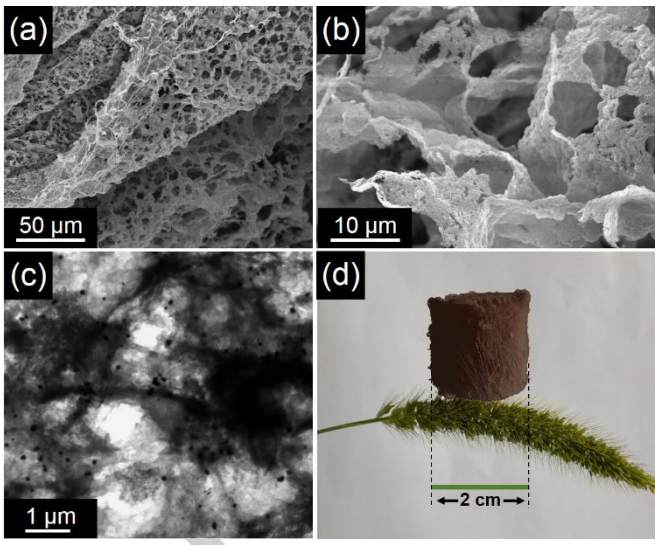

Figure 2. (a) Low- and (b) high-magnification scanning electron microscopy images of the Pt/MnO_2-BN20 aerogel. (c) TEM micrograph and (d) photograph of the Pt/MnO_2-BN20 aerogel.

Then, the SEM image of pure BN aerogel shown in **Figure S2** suggests that the BN sheets is connected through thin polymer layers. Meanwhile, the adsorption-desorption curve reveals a type-IV isotherm for BN aerogel (**Figure S4a**) and the corresponding surface area is up to 80. 05 m^2 g^{-1} (**Table S1**). Similarity, the interconnected highly porous Pt/MnO_2-BN aerogel materials are formed when polyvinyl alcohol (PVA) molecules act as a cross-linker to link the BN nanosheets. As displayed in **Figure 2a–b**, both the porous layered structure of the aerogel and the large BN sheet structure are obviously observed, which favors reactant and product transfer, thereby accelerating the oxidation of HCHO. Furthermore, the TEM micrograph demonstrates the Pt/MnO_2 composites to be evenly distributed across the BN nanosheets, confirming the successful anchoring of Pt/MnO_2 to the aerogels (**Figure 2c**). Additionally, SEM elemental mapping characterization demonstrates that B, N, O, Mn, and Pt are homogeneously distributed throughout the aerogel matrix (**Figure S3**), indicating the successful preparation of the Pt/MnO_2-BN aerogels herein. The Pt/MnO_2-BN20 aerogel possessing a fluffy and brown columnar macrostructure is presented in **Figure 2d**. As illustrated in **Figure S4b**, the N_2 adsorption-desorption isotherm of the Pt/MnO_2-BN20 catalyst exhibited a type-IV isotherm with a H3-type hysteresis loop. By connecting the various layers to an ordered porous structure, the interconnected network formed by the PVA molecules promotes the high surface area of BN and Pt/MnO_2-BN aerogels (**Table S1**). Furthermore, the Pt/MnO_2-BN20 catalyst exhibits a high surface area, which is beneficial for HCHO adsorption and in reducing the HCHO concentration during the catalytic oxidation process. Additionally, the inset of **Figure S4b** shows the pore size distributions, which exhibit primary modal pore sizes of *ca.* 3–5 nm, and with which reveals the existence of mesoporous structures in the aerogel catalysts. The HCHO uptake and storage capacities are significantly improved as a result of the enhanced effective surface areas and ordered porosity within the internal structure of the aerogels. Such enhanced properties improve the catalytic activity toward HCHO.

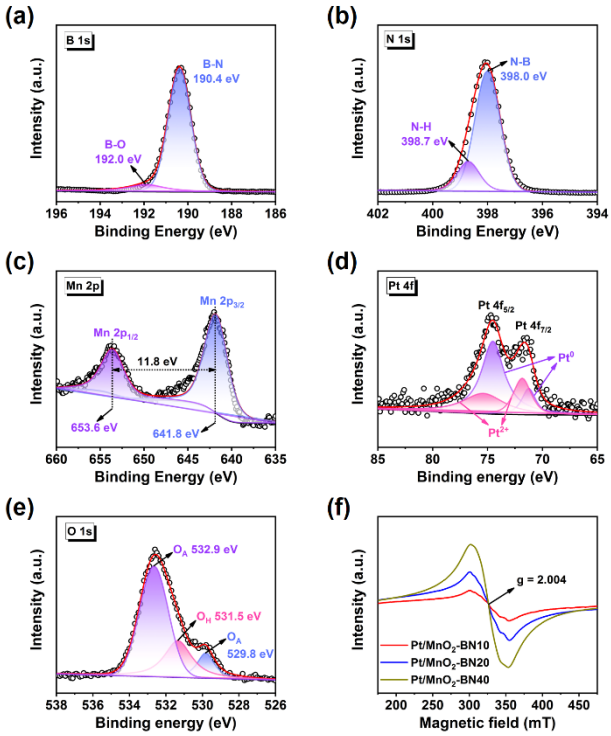

Figure 3. High-resolution X-ray photoelectron spectroscopy spectra for (a) B 1s, (b) N 1s, (c) Mn 2p, (d) Pt 4f, and (e) O 1s of the Pt/MnO_2-BN20 sample. (f) ESR spectra of the as-prepared Pt/MnO_2-BN10, Pt/MnO_2-BN20 and Pt/MnO_2-BN40 samples.

Extensive X-ray photoelectron spectroscopy (XPS) characterization was conducted to explore the surface element compositions and chemical states of the Pt/MnO_2-BN20 sample. The survey scan XPS spectrum shown in **Figure S5** reveals the existence of B, N, Mn, O and Pt elements in the Pt/MnO_2-BN20 sample, which is consistent with the elemental mapping analysis results (**Figure S3**). **Figure 3a-b** shows that the B 1s and N 1s spectra of the aerogel sample consist of two individual peaks, derived from BN, at binding energies (BE) = 190.4 eV, 192.0 eV and 398.0 eV, 398.7 eV, which are assigned to the B-N, B-O bonds and the N-B, N-H bonds, respectively.[6b, 14] **Figure 3c** shows that the Mn 2p signal of the sample can be divided into two peaks. The two strong peaks at BE = 641.83 eV and 653.63 eV, with a spin-energy separation of 11.8 eV, are assigned to Mn^{4+} and derive from the MnO_2 nanoflowers.[12] As illustrated in **Figure 3d**, the XPS spectrum of Pt 4f is deconvoluted into two main peaks at ~71.25 eV and 74.52 eV, which are assigned to the Pt $4f_{7/2}$ and Pt $4f_{5/2}$ binding energies, respectively. The Pt $4f_{7/2}$ signal relates to the two peaks at 71.25 eV and 71.84 eV. The Pt $4f_{5/2}$ signal comprises two components at 74.52 eV and 75.39 eV. The metallic Pt^0 at BE = 71.25 eV and 74.52 eV is most prominent.[6b, 12-13] The bands at 71.84 eV and 75.39 eV are attributed to Pt^{2+} species, such as PtO. Additionally, the actual Pt content in the Pt/MnO_2-BN20 sample is obtained through inductively coupled plasma-atomic emission spectroscopy measurements, as shown in **Table S1**. The actual values are observed to be slightly lower than the experimental-theoretical values as a result of the inevitable losses during the preparation process. The O 1s high-resolution spectrum, as observed in **Figure 3e,** comprises three peaks at 529.8, 531.5 and 532.9 eV, which can be attributed to lattice oxygen species (O_L), surface hydroxyl species (O_H) and surface adsorbed oxygen species (O_A), resprectively. Notably, the percentage of O_A is much higher than O_L and O_H, indicating the larger content of surface adsorbed oxygen species in Pt/MnO_2-BN20 sample. Besides, the result of calculated g value of ~2.004 from ESR test implies the presence of oxygen vacancies in the prepared Pt/MnO_2-BN10, Pt/MnO_2-BN20 and Pt/MnO_2-BN40 catalysts (**Figure 3f**). As reported in the literatures, numerous surface active O species onthe composite surface such as O_2^-, O^- and -OH group, which result from surface oxygen vacancies, play a significant role in oxidation reaction and are beneficial for HCHO oxidation.[13]

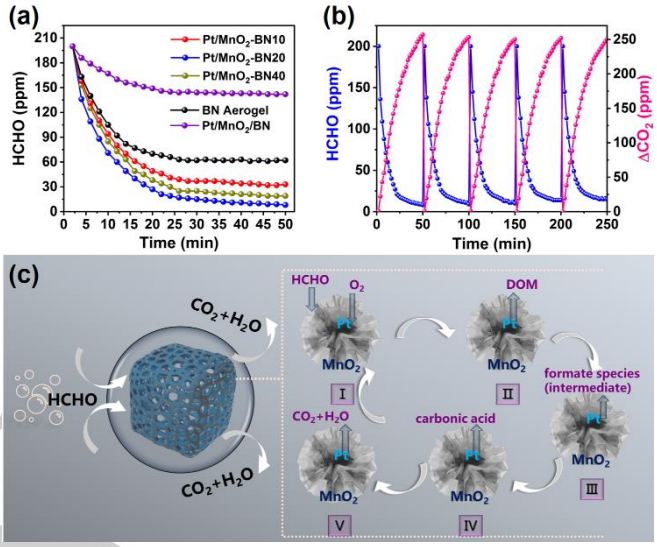

Figure 4. (a) Concentration changes of HCHO as a function of reaction time for the BN aerogel, Pt/MnO_2-BN and Pt/MnO_2/BN samples. (b) Real-time HCHO concentration and corresponding ΔCO_2 of the Pt/MnO_2-BN20 sample during five recycling tests. (c) Proposed reaction mechanism for HCHO oxidation over the Pt/MnO_2-BN catalysts.

The catalytic oxidation performance of the as-prepared Pt/MnO_2-BN10, Pt/MnO_2-BN20, Pt/MnO_2-BN40, Pt/MnO_2/BN and BN aerogel toward gaseous HCHO (200 ppm) conversion under an air atmosphere was investigated in detail. As displayed in **Figure 4a**, the pure BN aerogel is observed to have no catalytic effect at this experimental temperature. However, the HCHO concentration decreased and stabilized at 62 ppm after 25 min because of the strong adsorption capacity of the BN aerogel. Furthermore, the disordered Pt/MnO_2/BN catalyst prepared through simple mixing of Pt/MnO_2 and bulk BN exhibited worse HCHO catalytic performance. However, the Pt/MnO_2-BN aerogel materials clearly catalyze the degradation of HCHO with higher efficiencies, which implies the superiority of the porous aerogel structure. Among the Pt/MnO_2-BN aerogel catalysts, the HCHO concentration on Pt/MnO_2-BN20 catalyst decreases the fastest than those on Pt/MnO_2-BN10 and Pt/MnO_2-BN40. After 50 min, we can see that the HCHO concentration decrease from 200 ppm to 8, 19 and 33 ppm for Pt/MnO_2-BN20, Pt/MnO_2-BN40 and Pt/MnO_2-BN10, respectively. Importantly, the Pt/MnO_2-BN20 realizes a gaseous HCHO conversion of ~96% into harmless H_2O and CO_2 at room temperature, showing the highest catalytic activity. The superior catalytic performance of the Pt/MnO_2-BN20 catalyst derives from the optimum Pt/MnO_2 loading, the porous structure and the larger specific surface area of the aerogel. Therefore, the combination of catalytic oxidation with adsorption could significantly enhance the efficiency of HCHO treatment compared to adsorption or oxidation alone. The prepared

Pt/MnO_2-BN aerogel materials exhibited satisfactory catalytic performance toward removing HCHO in comparison with previously reported literatures in **Table S2**. Additionally, for practical applications, assessing the catalytic stability of Pt/MnO_2-BN20 is greatly significant. The catalyst cyclability toward the catalytic oxidation of HCHO was assessed by subjecting the catalyst to five reaction-regeneration cycles, as demonstrated in **Figure 4b**. The Pt/MnO_2-BN20 catalyst demonstrates excellent repeatability, even during the fifth cycle, where the HCHO removal rate is still maintained at ~92.5%. The BET result indicated Pt/MnO_2-BN20 sample remain the high surface area and mesoporous structure after the cycling tests (**Figure S4b** and **Table S1**). Meanwhile, the XRD patterns of the Pt/MnO_2-BN20 catalyst before and after the cycling tests were studied and are presented in **Figure S7**. No appreciable change was found in the crystalline structure, and the inset SEM image after the five cycling tests showed that the catalyst still has original mesoporous structure, further suggesting that the Pt/MnO_2-BN20 catalyst are relatively stable during the catalytic removal HCHO reaction. Besides, the obvious increase of the generated CO_2 concentration compared to the decrease of the entered HCHO concentration, which mainly result from the part of HCHO are desorbed from the surface of the reactor and then oxidized to CO_2.

Additionally, the mechanism for HCHO oxidation over the Pt/MnO_2-BN catalyst at room temperature is suggested in **Figure 4c** based on previous research. The porous layered structure structure together with large S_{BET} is beneficial to the diffusion of HCHO towards the catalyst surface. HCHO reactant gas molecules are first adsorbed onto the OH group of the MnO_2 substrate through hydrogen bonding. Simultaneously, O_2 molecules in the air are adsorbed onto and activated by negatively charged Pt NPs (step I), which can facilitate the subsequent oxidation of HCHO.[15] Moreover, the surface active oxygen (O_2^-, O^-, etc.) and structural hydroxyl groups play a vital role in this process. The consumed hydroxyls are regenerated by the dissociation of molecule water through the reaction of O_2^-, $O^- + H_2O \rightarrow$ 2-OH.[16] Then, the intermediate dioxymethylene (DOM) is generated through the process and the adsorbed HCHO molecules are oxidized by activated oxygen species (step II). Thereafter, DOM is quickly oxidized and transformed into formate species (intermediate) by activated oxygen species (step III). Next, intermediate formate species are further oxidized to unstable carbonic acid (step IV) that rapidly decomposes into harmless CO_2 and H_2O products. Meanwhile, the conversion of formates to CO_2 and H_2O is likely the rate-determining step in the whole process because the formate species were the main intermediates, With the continuous feeding of oxygen, the consumed O_2^- and O^- will be replenished by the activation of oxygen on the surface vacancies, such as oxygen vacancies (**Figure 3f)**, for further oxidation of formate species. Finally the products are released from the surface of the Pt/MnO_2-BN sample (step V) with the simultaneous regeneration of the catalyst active site. In short, harmful HCHO gas can undergo complete catalytic oxidation into harmless CO_2 and H_2O through the efficient Pt/MnO_2-BN catalyst.

In summary, a 3D Pt/MnO_2-BN catalyst was successfully fabricated through Pt NPs loading onto MnO_2 nanoflowers, followed by anchoring of the Pt/MnO_2 composites to BN aerogels. The porous structure is beneficial to the rapid transfer of reactants and products, thereby accelerating the HCHO oxidation process. Additionally, the combined adsorption and oxidation properties enhance the efficiency of the catalyst to reduce the HCHO concentration in air. Thus, the Pt/MnO_2-BN catalyst exhibits superior catalytic activity toward HCHO (200 ppm) achieving 96% conversion at room temperature. Furthermore, the 3D Pt/MnO_2-BN aerogel, as a monolithic catalyst, is easier to recycle and reuse in comparison with catalysts in powder form. The monolithic porous composite herein demonstrates promise as an oxidation catalyst and provides useful insights into the design of high-performance catalysts for room temperature HCHO removal.

Acknowledgements

We gratefully acknowledge the financial support provided by the National Natural Science Foundation of China (21938006, 51973148, 21722607, 21776190), Natural Science Foundation of the Jiangsu Higher Education Institutions of China (17KJA430014, 17KJA150009), and the project supported by the Priority Academic Program Development of Jiangsu Higher Education Institutions (PAPD).

Keywords: Pt/MnO_2 • boron nitride aerogel • formaldehyde • catalytic oxidation

[1] a) C. He, J. Cheng, X. Zhang, M. Douthwaite, S. Pattisson, Z. Hao, *Chem. Rev.* **2019**, *119*, 4471-4568; b) K. Silas, W. A. W. A. K. Ghani, T. S. Choong, U. Rashid, *Catal. Rev.* **2019**, *61*, 134-161; c) K. Vikrant, K.-H. Kim, A. Deep, *Appl. Catal. B- Environ.* **2019**, *259*, 118025.

[2] a) K. Wang, Y. Zeng, W. Lin, X. Yang, Y. Cao, H. Wang, F. Peng, H. Yu, *Carbon* **2020**, *167*, 709-717; b) W. Li, J. Wang, H. Gong, *Catal. Today* **2009**, *148*, 81-87.

[3] a) M. Chen, H. Yin, X. Li, Y. Qiu, G. Cao, J. Wang, X. Yang, P. Wang, *J. Hazard. Mater.* **2020**, 122628; b) W. Sun, Z. Yang, Y. Xu, Y. Shi, Y. Shen, G. Liu, *RSC Adv.* **2020**, *10*, 12772-12779; c) Y. Wang, J. Ye, C. Jiang, Y. Le, B. Cheng, J. Yu, *Environ. Sci.: Nano* **2020**, *7*, 198-209; d) M. F. Attia, M. I. Swasy, M. Ateia, F. Alexis, D. C. Whitehead, *Chem. Commun.* **2020**, *56*, 607-610; e) M. Zeng, Y. Li, M. Mao, J. Bai, L. Ren, X. Zhao, *ACS Catal.* **2015**, *5*, 3278-3286.

[4] a) K. Vikrant, M. Cho, A. Khan, K.-H. Kim, W.-S. Ahn, E. E. Kwon, *Environ. Res.* **2019**, *178*, 108672; b) J. Pei, J. S. Zhang, *Chem. Eng. J.* **2011**, *167*, 59-66; c) J. Yu, X. Li, Z. Xu, W. Xiao, *Environ. Sci. Technol.* **2013**, *47*, 9928-9933; d) T. Wang, Y. Wang, M. Sun, A. Hanif, H. Wu, Q. Gu, Y. S. Ok, D. C. Tsang, J. Li, J. Yu, *Chem. Sci.* **2020**, *11*, 6670-6681; e) L. Wang, X. Xu, Y. Wang, X. Wang, F.-n. Shi, *Inorg. Chem. Front.* **2018**, *5*, 1470-1476; f) L. Liu, H. Zhang, J. Jia, T. Sun, M. Sun, *Inorg. Chem.* **2018**, *57*, 8451-8457.

[5] a) S. Tanada, N. Kawasaki, T. Nakamura, M. Araki, M. Isomura, *J. Colloid Interf. Sci.* **1999**, *214*, 106-108; b) K. J. Lee, J. Miyawaki, N. Shiratori, S.-H. Yoon, J. Jang, *J. Hazard. Mater.* **2013**, *260*, 82-88; c) Z. Xu, J. Yu, J. Low, M. Jaroniec, *ACS Appl. Mater. Interfaces* **2014**, *6*, 2111-2117; d) J. Zhou, D. R. Mullins, *Surf. Sci.* **2006**, *600*, 1540-1546.

[6] a) X. Li, Y. Sun, T. Zhang, Y. Bai, X. Lyu, W. Cai, Y. Li, *Nanotechnology* **2019**, *30*, 105702; b) J. Ye, X. Zhu, B. Cheng, J. Yu, C. Jiang, *Environ. Sci. Technol. Lett.* **2017**, *4*, 20-25.

[7] a) K. K. Kang, L. H. Seok, L. Y. Hee, *Chem. Soc. Rev.* **2018**, *47*, 6342-6369; b) G. Bharath, K. Rambabu, A. Hai, H. Taher, F. Banat, *ACS Sustain. Chem. Eng.* **2020**, *8*, 7278-7289; c) H. Chen, S.-Z. Yang, Z. Yang, W. Lin, H. Xu, Q. Wan, X. Suo, T. Wang, D.-e. Jiang, J. Fu, *ACS Cent. Sci.* **2020**, *6*, 1617-1627; d) X. Zhang, Y. Gao, *Chem-Asian J.*

2020, *15*, 1315-1323; e) W. Lei, D. Portehault, D. Liu, S. Qin, Y. Chen, *Nat. Commun.* **2013**, *4*, 1-7.

[8] a) C. Zhang, H. He, *Catal. Today* **2007**, *126*, 345-350; b) B. Liu, Y. Liu, C. Li, W. Hu, P. Jing, Q. Wang, J. Zhang, *Appl. Catal. B-Environ.* **2012**, *127*, 47-58; c) H. Huang, D. Y. Leung, *ACS Catal.* **2011**, *1*, 348-354.

[9] a) Z. Huang, X. Gu, Q. Cao, P. Hu, J. Hao, J. Li, X. Tang, *Angew. Chem. Int. Ed.* **2012**, *51*, 4198-4203; b) L. Ma, D. Wang, J. Li, B. Bai, L. Fu, Y. Li, *Appl. Catal. B-Environ.* **2014**, *148*, 36-43; c) L. Zhou, J. He, J. Zhang, Z. He, Y. Hu, C. Zhang, H. He, *J Phys. Chem. C* **2011**, *115*, 16873-16878; d) L. Liu, J. Sun, J. Ding, Y. Zhang, J. Jia, T. Sun, *Inorg. Chem.* **2019**, *58*, 14275-14283.

[10] a) C. Zhang, F. Liu, Y. Zhai, H. Ariga, N. Yi, Y. Liu, K. Asakura, M. Flytzani‐Stephanopoulos, H. He, *Angew. Chem. Int. Ed.* **2012**, *51*, 9628-9632; b) X. Tang, J. Chen, X. Huang, Y. Xu, W. Shen, *Appl. Catal. B-Environ.* **2008**, *81*, 115-121; c) C. Zhang, Y. Li, Y. Wang, H. He, *Environ. Sci. Technol.* **2014**, *48*, 5816-5822.

[11] a) X. Tang, Y. Li, X. Huang, Y. Xu, H. Zhu, J. Wang, W. Shen, *Appl. Catal. B-Environ.* **2006**, *62*, 265-273; b) R. Fang, H. Huang, J. Ji, M. He, Q. Feng, Y. Zhan, D. Y. Leung, *Chem. Eng. J.* **2018**, *334*, 2050-2057; c) L. Lu, H. Tian, J. He, Q. Yang, *J. Phys. Chem. C* **2016**, *120*, 23660-23668.

[12] J. Liu, L. Meng, Z. Fei, P. J. Dyson, L. Zhang, *Biosens. Bioelectron.* **2018**, *121*, 159-165.

[13] J. Ye, M. Zhou, Y. Le, B. Cheng, J. Yu, *Appl. Catal. B-Environ.* **2020**, *267*, 118689.

[14] P. S. Owuor, O.-K. Park, C. F. Woellner, A. S. Jalilov, S. Susarla, J. Joyner, S. Ozden, L. Duy, R. Villegas Salvatierra, R. Vajtai, *ACS Nano* **2017**, *11*, 8944-8952.

[15] S. Huang, X. Zhu, B. Cheng, J. Yu, C. Jiang, *Environ. Sci.: Nano* **2017**, *4*, 2215-2224; b) P. Zhou, J. Yu, L. Nie, M. Jaroniec, *J. Mater. Chem. A* **2015**, *3*, 10432-10438; c) J. Ji, X. Lu, C. Chen, M. He, H. Huang, *Appl. Catal. B-Environ.* **2020**, *260*, 118210.

[16] J. Wang, P. Zhang, J. Li, C. Jiang, R. Yunus, J. Kim, *Environ. Sci. Technol.* **2015**, *49*, 12372-12379; b) M. Wang, L. Zhang, W. Huang, T. Xiu, C. Zhuang, J. Shi, *Chem. Eng. J.* **2017**, *320*, 667-676.

10.1002/anie.202013667

Entry for the Table of Contents

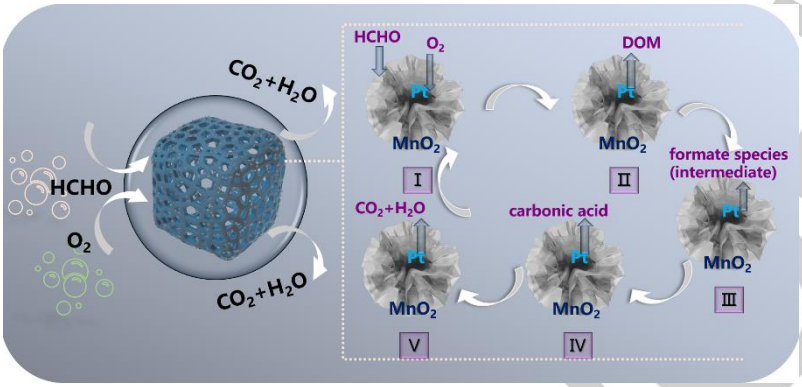

Three-dimensional monolithic Pt/MnO_2-BN catalyst was successfully fabricated by anchoring Pt/MnO_2 nanoflower on boron nitride (BN) aerogels. The as-formed porous aerogels catalyst possesses the excellent ability of the combination of adsorption and oxidation to effecient removal of formaldehyde at room temperature, as well as easier to be recycled and reused in comparison with powdery ones.